Adaptive Multisensor Acquisition via Spatial Contextual Information for Compressive Spectral Image Classification

Nelson Diaz ⓘ , *Member, IEEE*, Juan Ramirez ⓘ , *Member, IEEE*, Esteban Vera ⓘ , *Member, IEEE*, and Henry Arguello ⓘ , *Senior Member, IEEE*

Abstract—Spectral image classification uses the huge amount of information provided by spectral images to identify objects in the scene of interest. In this sense, spectral images typically contain redundant information that is removed in later processing stages. To overcome this drawback, compressive spectral imaging (CSI) has emerged as an alternative acquisition approach that captures the relevant information using a reduced number of measurements. Various methods that classify spectral images from compressive projections have been recently reported whose measurements are captured by nonadaptive, or adaptive schemes discarding any contextual information that may help to reduce the number of captured projections. In this article, an adaptive compressive acquisition method for spectral image classification is proposed. In particular, we adaptively design coded aperture patterns for a dual-arm CSI acquisition architecture, where the first system obtains compressive multispectral projections and the second arm registers compressive hyperspectral snapshots. The proposed approach exploits the spatial contextual information captured by the multispectral arm to design the coding patterns such that subsequent snapshots acquire the scene's complementary information improving the classification performance. Results of extensive simulations are shown for two state-of-the-art databases: Pavia University and Indian Pines.

Furthermore, an experimental setup that performs the adaptive sensing was built to test the performance of the proposed approach on a real dataset. The proposed approach exhibits superior performance with respect to other methods that classify spectral images from compressive measurements.

Index Terms—Adaptive acquisition, compressive spectral imaging, spatial contextual information, spectral image classification.

I. INTRODUCTION

SPECTRAL image (SI) classification is an important topic in remote sensing that aims at assigning predefined labels to the corresponding SI pixels. It has been widely used to detect and characterize materials in a scene of interest given the huge amount of discriminative spatial-spectral information provided by SIs. In particular, SI classification has been used in various remote sensing applications such as forest classification [1], monitoring of agricultural land use [2], and precision agriculture [3]. In the last two decades, different pixel-based classification approaches have been proposed to label SIs, including methods based on support vector machines (SVMs) [4], random forest (RF) [5], [6], neural networks [7], dictionary-based sparse representation [8], and multinomial logistic regression [9].

In general, pixel-based classification techniques suffer the so-called curse of dimensionality [10] degrading the labeling accuracy as the number of spectral bands increases due to the limited availability of training samples. To overcome this drawback, various classification approaches resort to either dimensionality reduction (DR) or feature extraction techniques, assuming that the relevant information embedded in spectral signatures lives in a low-dimensional space. Principal component analysis (PCA) [11], independent component analysis (ICA) [12], and kernel-based methods [13], [14] are just few examples of traditional DR approaches. Furthermore, different techniques that extract the spatial contextual information (SCI) have been used to improve the labeling accuracy, minimizing the salt and pepper noise in classification maps [9], [15]–[17]. Recently, various optimization-based and deep learning-based feature extraction methods (supervised and unsupervised) have been developed yielding low-dimensional attributes for hyperspectral image classification [18], [19]. However, spectral image classification methods are typically applied to datasets acquired

by scanning sensors that obtain the entire image based on the Nyquist sampling theorem [20], leading to a high demand in storage and transmission during the acquisition process.

In this regard, compressive spectral imaging (CSI) has become a compressive sensing-based acquisition framework that captures the relevant information in spectral images using a reduced set of measurements [20]. The most representative CSI architecture was presented by Wagadarikar *et al.* in [21]—namely, the coded aperture snapshot spectral imager (CASSI)—which modulates and disperses the spectral density source before it impinges into a camera detector. Furthermore, different variants of the CASSI system has been proposed such as the dual disperser CASSI (DD-CASSI) [22], the 3-D-CASSI [20], and the colored-CASSI [23]. In addition, a multisensor CSI architecture was recently implemented to recover high-resolution spectral images from hyperspectral and multispectral compressive samples [24], [25].

An intuitive classification approach would involve the image reconstruction from compressive measurements, and then, the labeling map is obtained by applying a pixel-based classifier to the reconstructed spectral image. In this sense, Ramirez *et al.* proposed a classification method from CASSI projections. Particularly, this method includes a reconstruction algorithm that recover the PCA coefficients of the spectral image and the labeling is performed using the nearest neighbor method [26]. This method is severely affected by classification noise and it is computationally demanding. A classification method in the compressive domain is also reported in [27] that is relied on an adaptive sensing scheme [22]. This approach consists of an adaptive coded aperture design method based on the Bayesian classifier. However, this technique is tailored to the DD-CASSI architecture, and its extension to other CSI sensors has become a challenging task.

On the other hand, feature fusion for imagery classification from multisensor data has become an important topic in the last few years due to the large volume of information captured by diverse remote sensing systems [28], [29]. However, these methods have been designed to fuse multisensor data captured by conventional acquisition systems, challenging the storage and computing capabilities of processing systems. Various land cover classification approaches from multisensor compressive measurements have been recently proposed in [30]–[32]. These approaches obtain the target fused features by solving regularized optimization problems and the labeling maps are obtained from fused features by using pixel-based classifiers. Nonetheless, these methods require capturing the entire sample set for a given compression ratio. On the other hand, adaptive compressive acquisition schemes that minimize the number of required samples to achieve a high-quality reconstruction have also been developed [33]–[35]. In this way, an adaptive multisensor acquisition scheme that considers the local spatial information in spectral images can be designed to reduce even further the number of necessary measurements to achieve a competitive labeling performance.

In this work, we aim to develop an adaptive acquisition framework based on a multi-sensor compressive system for land cover classification. In this sense, the proposed approach focuses on capturing the relevant scene information to reduce the number of measurements required for achieving the desired labeling accuracy. In contrast to previous approaches that classify spectral images from compressive measurements, the proposed method includes an adaptive acquisition scheme designed to improve the labeling performance. Moreover, the proposed adaptive method does not solve a computationally costly optimization problem to extract classification features from compressive projections. Instead, this acquisition scheme uses the spatial contextual information in spectral images to adaptively design the coded aperture patterns of a compressive multisensor system equipped with two CSI optical architectures. The proposed adaptive sensing is evaluated on the 3-D-CASSI [20] and the C-CASSI [23]. As far as we know, no other CSI systems are currently performing adaptive CSI acquisition for SI classification. The contributions of this article are threefold.

1) We develop an adaptive acquisition method to capture multisensor compressive measurements to classify high-resolution spectral images without resorting to a spectral image reconstruction algorithm. More precisely, the proposed acquisition approach first takes advantage of the spatial contextual information embedded in MS projections to adaptively design the colored coded aperture patterns of a multisensor compressive optical system.

2) Second, we propose an algorithm that extracts classification features from adaptive compressive measurements. This algorithm attains outstanding classification results for a reduced set of multisensor compressive projections, and it also remarkably improves the labeling accuracy as the number of compressive snapshots increase.

3) The proposed approach outperforms other classification methods from compressive measurements.

This article is organized as follows. Section II presents the observation model, which describes the optical model comprised of a dual-arm C-CASSI and 3-D-CASSI system. Section III describes the proposed adaptive CSI classification scheme. Section IV outlines the results using the adaptive approach using synthetic and experimental hyperspectral datasets. Conclusions are summarized in Section V.

II. Observation Model

Notice that the proposed classification method is applied to compressive measurements captured by dual-arm systems based on the 3-D-CASSI [20] and the C-CASSI [23] optical architectures. Therefore, we start by presenting a brief description of the CASSI-based sensors. Afterward, we introduce the proposed dual-arm architecture comprised of a high spatial resolution system and a high spectral resolution system. A specific description of the dual-arm-based 3-D-CASSI and C-CASSI is presented in this section.

A. CASSI-Based Optical Architectures

In order to describe the CASSI-based optical systems, consider $f_0(x, y, \lambda)$ as the spectral density source associated with

the scene of interest, where (x, y) represents the spatial location and λ denotes a particular wavelength. In particular, CASSI-based architectures encode the spectral density source by including a coded aperture that typically consists of an array of optical filters. In this sense, the encoded spectral density can be described as

$$f_1(x, y, \lambda) = f_0(x, y, \lambda)t(x, y, \lambda) \tag{1}$$

where $t(x, y, \lambda)$ is a function that describes the spatial-spectral encoding operation performed by the coded aperture. Then, the encoded field is spectrally shifted by a dispersive element. Thus, the encoded-and-shifted spectral field is given by

$$f_2(x, y, \lambda) = \iiint f_1(x', y', \lambda') \\ \times h(x - \psi(\lambda) - x', y - y', \lambda - \lambda')dx'dy'd\lambda' \tag{2}$$

where $h(x, y, \lambda)$ is the impulse response of the optical system, and $\psi(\lambda)$ describes the shifting effect induced by the optical dispersive element. In general, the sensor's impulse response is assumed as the Dirac delta function, i.e., $h(x, y, \lambda) = \delta(x, y, \lambda)$. Furthermore, it is worth noting that the 3-D CASSI system does not contain the dispersive element [20], therefore, for this system, it is assumed that $\psi(\lambda) = 0$. Subsequently, the encoded-and-dispersed spectral field is integrated over the spectral sensitivity of the detector plane. In this regard, the projected plane can be expressed as

$$g(x, y) = \int_\Lambda f_2(x, y, \lambda). \tag{3}$$

Moreover, let Δ be the pixel width of the camera detector; thus, the intensity captured by the detector at the discrete coordinate (i, j) can be described as

$$(\mathbf{Y})_{(i,j)} = \int_\Delta \int_\Delta g(x, y)\text{rect}\left(\frac{x}{\Delta} - i, \frac{y}{\Delta} - j\right)dxdy \tag{4}$$

where $\text{rect}(\frac{x}{\Delta} - i, \frac{y}{\Delta} - j)$ represents the area covered by the detector pixel at the spatial location (i, j). The expression of the intensity captured by a CASSI-based detector at the location (i, j) is described by the discrete model shown as follows:

$$(\mathbf{Y})_{i,j} = \sum_{\ell=0}^{L-1} \mathcal{F}_{i,(j-c\ell),\ell}\mathcal{T}_{i,(j-c\ell),\ell} + \eta_{i,j} \tag{5}$$

where $\mathcal{F} \in \mathbb{R}^{M \times N \times L}$ is a discrete version of the input spectral image with dimensions of $M \times N$ pixels and L spectral bands. Every element of the input spectral image is denoted as $\mathcal{F}_{i,j,\ell}$ with ℓ as the spectral index. Notice that $\mathcal{T} \in \{0, 1\}^{M \times N \times L}$ is a binary cube with entries $\mathcal{T}_{i,j,\ell}$ that describes the spatial-spectral encoding operation performed by the coded aperture; $\eta_{i,j}$ is the noise inherent to the sampling system; and c is a factor related to the spectral shifting operation induced by the dispersive element which typically is set to $c = 1$ for C-CASSI.

Multiple snapshots are frequently required to reconstruct a reliable version of the discrete spectral image from CASSI compressive measurements, where each snapshot is captured
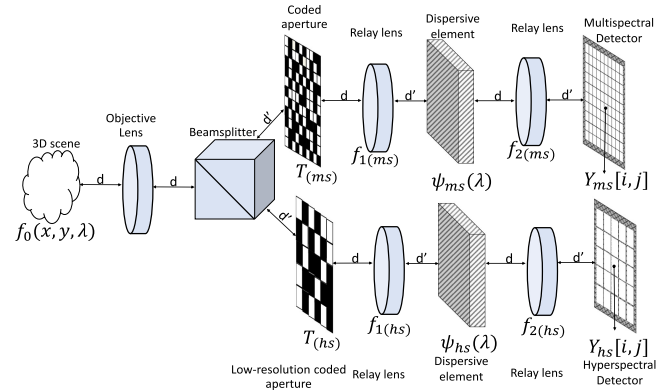

Fig. 1.   Schematic of the dual-arm architecture based on the colored-CASSI optical system with a multispectral sensor and a hyperspectral sensor.

using a different encoding pattern. Hence, the intensity captured at the coordinate (i, j) and the kth snapshot can be given by

$$(\mathbf{Y})_{i,j}^k = \sum_{\ell=0}^{L-1} \mathcal{F}_{i,(j-c\ell),\ell}\mathcal{T}_{i,(j-c\ell),\ell}^k + \eta_{i,j}^k \tag{6}$$

for $k = 0, \ldots, K$, where K is the number of captured snapshots and $\mathcal{T}^k \in \{0, 1\}^{M \times N \times L}$ is the binary model of a distinct encoding pattern used at the kth snapshot. Finally, the vectorized CASSI compressive measurements can be obtained as

$$\mathbf{y} = \mathbf{Hf} + \boldsymbol{\eta} \tag{7}$$

where $\mathbf{y} \in \mathbb{R}^{M(N+cL-c)K}$ is the vector that contains the set of compressive samples; $\mathbf{H} \in \mathbb{R}^{M(N+cL-c)K \times (MNL)}$ denotes the matrix that describes the acquisition process including the encoding operation performed by the coded aperture, the dispersive element effect, and the projection onto the camera detector; $\mathbf{f} \in \mathbb{R}^{MNL}$ is the input spectral image in vector form; and $\boldsymbol{\eta} \in \mathbb{R}^{M(N+cL-c)K}$ is the additive noise vector.

B. Dual-Arm Architecture Based on C-CASSI

Fig. 1 illustrates a representation scheme of the dual-arm architecture based on the C-CASSI optical system. As can be seen, the beamsplitter divides the input spectral density into two optical paths. The upper arm, which is referred to as the multispectral arm, is a C-CASSI sensor that contains two relay lenses, a dispersive element, a high-spatial-resolution coded aperture, and a high-spatial-resolution detector plane. On the other hand, the bottom arm called the hyperspectral arm is a C-CASSI system equipped with a low-spatial-resolution coded aperture and a low-spatial-resolution camera detector.

This article proposes a spectral image classification method from compressive measurements captured by the dual-arm system. More precisely, the measurements captured by the dual-arm system are adaptively obtained by considering the spatial contextual information of the scene of interest with the aim of improving the classification performance using a reduced set of measurements. To this end, we also propose two algorithms that adaptively design the encoding patterns of both the multispectral

arm coded aperture and the hyperspectral arm code aperture. Therefore, the multispectral arm and hyperspectral arm acquisition processes for the C-CASSI is described next.

C-CASSI multispectral arm: This branch captures high-spatial but low-spectral resolution compressive samples. More precisely, the compressive measurements obtained by the C-CASSI multispectral arm can be modeled as

$$\overline{\mathbf{y}}_{(ms)} = \overline{\mathbf{H}}_{(ms)}\mathbf{D}_{(ms)}\mathbf{f} + \boldsymbol{\eta}_{(ms)} \tag{8}$$

where $\overline{\mathbf{H}}_{(ms)}$ is the measurement matrix of the compressive multispectral arm and $\mathbf{D}_{(ms)} \in \mathbb{R}^{\frac{MNL}{q} \times MNL}$ is the downsampling matrix of that reduces the number of spectral bands with γ as the spectral decimation factor. The measurement matrix that describes the acquisition system at the kth snapshot $\overline{\mathbf{H}}_{(ms)}^{k}$ can be defined as

$$\overline{\mathbf{H}}_{(ms)}^{k} =$$
$$\begin{pmatrix} \mathbf{T}_{(ms)}^{(k,1)} & \mathbf{0}_{M(1)\times MN} & \cdots & \mathbf{0}_{M(L-1)\times MN} \\ \vdots & \mathbf{T}_{(ms)}^{(k,2)} & \cdots & \vdots \\ \vdots & \vdots & \ddots & \vdots \\ \mathbf{0}_{M(L-1)\times MN} & \mathbf{0}_{M(L-2)\times MN} & \cdots & \mathbf{T}_{(ms)}^{(k,\frac{L}{q})} \end{pmatrix} \tag{9}$$

where $\mathbf{T}_{(ms)}^{(k,\ell)} = \operatorname{diag}(\boldsymbol{\mathcal{T}}_{:,:,\ell}^{(ms)})$ is the diagonalized version of the ℓth band extracted from the binary model that describes the coded aperture used by the compressive multispectral arm at the kth snapshot, and $\mathbf{0}_{M \times N}$ is a matrix with dimensions $M \times N$ whose entries are zero. It is worth noting that the proposed approach adaptively designs the measurement matrices, and consequently the coded aperture patterns, to improve the image classification performance.

On the other hand, the multispectral decimation matrix can be defined by $\mathbf{D}_{(ms)} = \mathbf{D}_{\lambda} \otimes \mathbf{I}_{MN}$, being $\mathbf{D}_{\lambda} \in \mathbf{R}^{\frac{L}{q} \times L}$ the matrix that averages the spectral bands of the original datacube, $\otimes$ denotes the Kronecker product, and $\mathbf{I}_{MN} \in \mathbb{R}^{MN \times MN}$ is an identity matrix. Notice that the multispectral image can be obtained as $\mathbf{f}_{(ms)} = \mathbf{D}_{(ms)}\mathbf{f}$, and $\boldsymbol{\eta}_{(ms)}$ is the additive noise vector that contaminates the compressive multispectral samples.

C-CASSI hyperspectral arm: This arm acquires low-spatial resolution compressive measurements with rich spectral information. In particular, the compressive samples captured by the hyperspectral arm can be succinctly described as

$$\overline{\mathbf{y}}_{(hs)} = \overline{\mathbf{H}}_{(hs)}\mathbf{D}_{(hs)}\mathbf{f} + \boldsymbol{\eta}_{(hs)} \tag{10}$$

where $\overline{\mathbf{H}}_{(hs)}$ is the measurement matrix of the compressive hyperspectral arm, $\mathbf{D}_{(hs)} \in \mathbb{R}^{\frac{MNL}{p^2} \times MNL}$ is the downsamplig matrix with p as the spatial decimation factor, and $\boldsymbol{\eta}_{(hs)}$ is the additive noise vector. In this case, the measurement matrix that characterizes the compressive acquisition process at the kth

snapshot can be modeled as

$$\overline{\mathbf{H}}_{(hs)}^{k} =$$
$$\begin{pmatrix} \mathbf{T}_{(hs)}^{(k,1)} & \mathbf{0}_{\frac{M}{p}(1)\times\frac{MN}{p^2}} & \cdots & \mathbf{0}_{\frac{M}{p}(L-1)\times\frac{MN}{p^2}} \\ \mathbf{0} & \mathbf{T}_{(hs)}^{(k,2)} & \cdots & \mathbf{0} \\ \vdots & \vdots & \ddots & \vdots \\ \mathbf{0}_{\frac{M}{p}(L-1)\times\frac{MN}{p^2}} & \mathbf{0}_{\frac{M}{p}(L-2)\times\frac{MN}{p^2}} & \cdots & \mathbf{T}_{(hs)}^{(k,L)} \end{pmatrix} \tag{11}$$

where $\mathbf{T}_{(hs)}^{(k,\ell)} = \operatorname{diag}(\boldsymbol{\mathcal{T}}_{:,:,\ell}^{(hs)})$ is the diagonalized version of the ℓth band extracted from the binary model that characterizes the coded aperture used by the compressive hyperspectral arm at the kth snapshot. A detailed description of $\mathbf{D}_{(hs)}$ is presented below.

1) The spatial decimation matrix $\mathbf{D}_{(hs)} \in \mathbb{R}^{\frac{MNL}{p^2} \times MNL}$ can be described as $\mathbf{D}_{(hs)} = \mathbf{I}_{(hs)} \otimes \mathbf{S}_{(hs)}$ where $\mathbf{I}_{(hs)} \in \mathbb{R}^{L \times L}$ is an identity matrix, and $\mathbf{S}_{(hs)} \in \mathbb{R}^{\frac{MN}{p^2} \times MN}$, it is a matrix that degrades spatially each band, it is given by $\mathbf{S}_{(hs)} = \mathbf{D}_c\mathbf{D}_r$.

2) The matrix $\mathbf{D}_c \in \mathbb{R}^{\frac{MN}{p^2} \times \frac{MN}{p}}$ decimates the columns of each spectral band. In more detail, $\mathbf{D}_c = \mathbf{I}_c \otimes \mathbf{G}^T$ where $\mathbf{G}^T \in \mathbb{R}^{\frac{N}{p} \times N}$ is given by $G_l = \boldsymbol{\Theta}_c^{(l)}\mathbf{d}_c$ where $l = \{0, 1\cdots, \frac{N}{p} - 1\}$ corresponds to the index of the columns of matrix $\mathbf{G}$, $\mathbf{d}_c \in \mathbb{R}^N$ is a vector that selects of columns, the position of the ones are determined by $\frac{iN}{p}$ with $i = \{0, 1\cdots, p-1\}$ and $\boldsymbol{\Theta}_c^{(l)} \in \mathbb{R}^{N \times N}$ is a permutation matrix is given by

$$\boldsymbol{\Theta}_c = \begin{pmatrix} 0 & 0 & \cdots & 0 & 1 \\ 1 & 0 & \cdots & 0 & 0 \\ 0 & 1 & \cdots & 0 & 0 \\ \vdots & \vdots & \ddots & \vdots & \vdots \\ 0 & 0 & \cdots & 1 & 0 \end{pmatrix}. \tag{12}$$

3) The matrix $\mathbf{D}_r \in \mathbb{R}^{\frac{MN}{p} \times MN}$ decimate the rows of each spectral band, which is given by $\mathbf{D}_r = \mathbf{I}_r \otimes \mathbf{d}_r$ where $\mathbf{d}_r = \mathbf{1}^T$ is a vector of all ones such as $\mathbf{d}_r \in \mathbb{R}^p$.

C. Dual-Arm Architecture Based on 3-D-CASSI

The compressive measurements of the 3-D-CASSI preserve better the spatial distribution of the acquired projection than the C-CASSI compressive measurements. The compressive measurements of 3D-CASSI are given by (6) when $c = 0$, denoting the absence of dispersion in the system. In the following are presented the measurement matrix of the multispectral arm and hyperspectral arm.

3-D-CASSI multispectral arm: The compressive samples captured by the 3-D-CASSI multispectral arm can be also expressed by (8), using the following the measurement matrix representing the acquisition system at the kth snapshot is defined as

$$\overline{\mathbf{H}}_{(ms)}^{k} = \left[\mathbf{T}_{(ms)}^{(k,1)}, \mathbf{T}_{(ms)}^{(k,2)}, \ldots, \mathbf{T}_{(ms)}^{(k,\frac{L}{q})}\right] \tag{13}$$
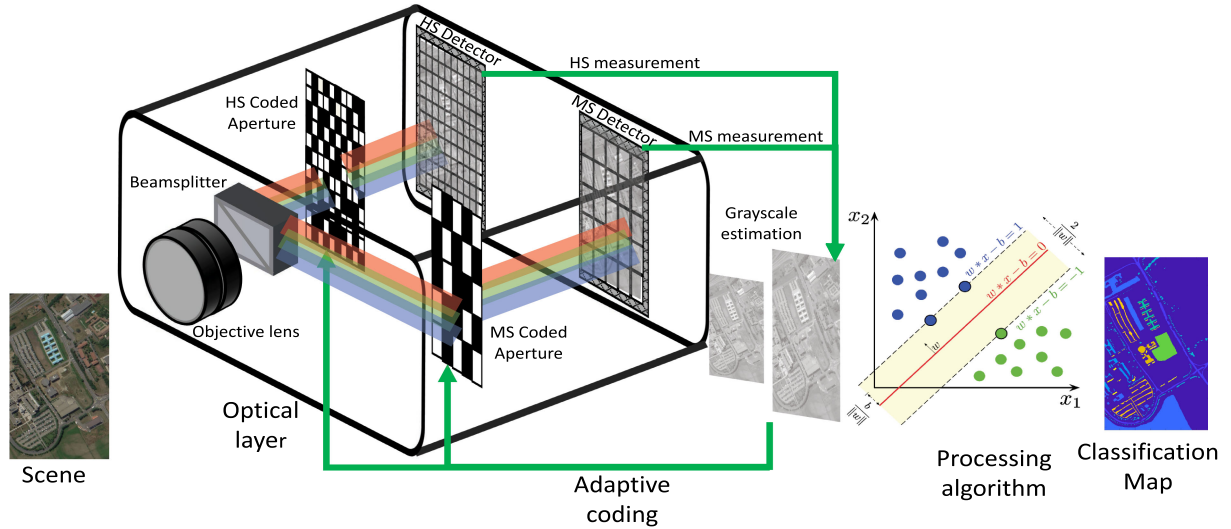
Fig. 2. Sketch of the optical and processing algorithm of the 3-D-CASSI. In the optical layer, the light of the scene enters through the objective lens. After that, the incoming light is divided by the beamsplitter. Thus, the beam in each arm is encoded by the coded aperture and multiplexed onto the detector. The compressive measurements are used to estimate the grayscale image of the scene. The subsequently coded apertures are computed using the contextual spatial information of the grayscale image estimation. At the end of the sensing process, the processing algorithm computes the classification map.

where (8) exhibits no dispersion, when the corresponding measurement matrix is replaced by (13). The resulting compressive multispectral measurements are given by $\overline{\mathbf{y}}_{(\mathrm{ms})}^k = \overline{\mathbf{H}}_{(\mathrm{ms})}^k \mathbf{D}_{(\mathrm{ms})} \mathbf{f} + \boldsymbol{\eta}_{(\mathrm{ms})}$, where $\mathbf{D}_{(\mathrm{ms})}$ represents the decimation along the spectral axis, $\mathbf{f}$ is the underlying datacube, and $\boldsymbol{\eta}_{(\mathrm{ms})}$ is the additive noise in the multispectral sensor.

3-D-CASSI hyperspectral arm: The compressive measurements obtained by the 3-D-CASSI hyperspectral branch can be represented by (10), utilizing the sampling matrix at the kth snapshot can be described as

$$\overline{\mathbf{H}}_{(\mathrm{hs})}^k = \left[\mathbf{T}_{(\mathrm{hs})}^{(k,1)}, \mathbf{T}_{(\mathrm{hs})}^{(k,2)}, \ldots, \mathbf{T}_{(\mathrm{hs})}^{(k,L)} \right] \qquad (14)$$

such that (10) denotes no dispersion, when the associated measurement matrix is substituted by (14). The resulting compressed hyperspectral measurements are given by $\overline{\mathbf{y}}_{(\mathrm{hs})}^k = \overline{\mathbf{H}}_{(\mathrm{hs})}^k \mathbf{D}_{(\mathrm{hs})} \mathbf{f} + \boldsymbol{\eta}_{(\mathrm{hs})}$, where $\mathbf{D}_{(\mathrm{hs})}$ denotes the decimation along the spatial dimensions, $\mathbf{f}$ is the underlying datacube, and $\boldsymbol{\eta}_{(\mathrm{hs})}$ is the additive noise in the hyperspectral detector.

III. DESIGN OF ADAPTIVE ACQUISITION

To perform the adaptive acquisition is required to compute the contextual information of the scene. The contextual spatial information is used to design the coded apertures. This section describes the hardware and processing algorithm that computes the contextual spatial information and the adaptive coded aperture design. In particular, Fig. 2 shows the optical and the processing algorithm that allows attaining the compressive measurements and the classification maps, respectively.

A. Computation of the Contextual Information

1) Grayscale Image Estimation: The grayscale image is estimated to design the coded aperture by exploiting the spatial

resolution in the multispectral arm. The intuition is to reduce the dispersion in the captured measurement. The acquisition of the grayscale is different depending on the CSI architecture. For the 3-D-CASSI, the colored coded aperture of the first snapshot in the multispectral arm is set to an all-ones matrix $\mathcal{T}_{i,j,\ell,0}^{(ms)} = 1$, exploiting the lack of disperser. This structure has the same effect as removing the coded aperture. For the C-CASSI, the dispersion is reduced using a colored coded aperture with bandpass filter $\mathcal{T}_{i,j,m,0}^{(ms)} = 1$ in all the spatial position, where m denotes the middle wavelengths. The bandpass filter samples the central wavelengths. The purpose of this step is to attain the first multispectral compressive measurement $\mathbf{Y}_{(\mathrm{ms})}^0$ with lower dispersion or approximately a grayscale image. Equation (6) denotes the acquisition of first and successive compressive measurements. In C-CASSI, the compressive measurements are cropped to retain the scene's spatial size. The contextual spatial information is obtained from the estimated grayscale images using two processes, high-pass filtering, and quantization.

2) High-Pass Filter: The high-pass filtering process obtains the components of the high frequency of the estimated grayscale image $\overline{\mathbf{Y}}_{(\mathrm{ms})}^0$, i.e., detecting the edge of the estimated grayscale image. The filtering is computed using $\overline{\mathbf{Y}}_{(ms)(i,j)}^0 = \sum_{i=0}^{M-1} \sum_{j=0}^{N-1} h_{(i-u,j-v)} \mathbf{Y}_{(ms)(i,j)}^0$, where $\overline{\mathbf{Y}}_{(ms)(i,j)}^0$ is the output image of the high pass filtering, $h_{(i,j)}$ is the filter impulse response, $\mathbf{Y}_{(ms)(i,j)}^0$ is the compressive measurement.

3) Quantization: In the quantization stage, the filtered image $(\overline{\mathbf{Y}})_{(ms)(i,j)}^0$ is quantized according to the number of classes in the scene n_c. Due to our approach is supervised n_c is known, then it is assumed that the step size in the quantizer $\gamma = n_c$. The typical quantizer can be seen as segmentation method $(\boldsymbol{\Gamma})_{(\mathrm{ms})(\mathrm{i,j})} = \gamma \lfloor \frac{(\overline{\mathbf{Y}})_{(ms)(i,j)}^0}{\gamma} + \frac{1}{2} \rfloor$, where $\lfloor \cdot \rfloor$ is the floor function, γ is the quantizer's step size. The matrix

---

Algorithm 1: Classification Using Adaptive Coded Aperture Design, and Exploiting Spatial Contextual Information in a Multisensor CSI.

Input: $\mathbf{Y}^0_{(ms)}$ ▷ Inputs of the algorithm.
Output: $\mathbf{C}_{test}$.   ▷ Output of the algorithm.

1:   **function** CLASSIFICATION USING ADAPTIVE CODING $\mathbf{Y}^0_{(ms)}$

2:   $\overline{\mathbf{Y}}^0_{(ms)} \leftarrow \mathbf{High-passfilter}(\mathbf{Y}^0_{(ms)})$ ▷ High-pass filtering of grayscale image.

3:   $\boldsymbol{\Gamma}_{(ms)} \leftarrow \mathbf{Quantization}(\overline{\mathbf{Y}}^0_{(ms)})$ ▷ Quantization of grayscale image.

4:   $\mathbf{M}_{(ms)} \leftarrow \mathbf{E}_{(ms)}\mathbf{I}_{(ms)} \otimes \mathbf{1}_{(ms)}$ ▷ Matched filter in MS arm.

5:   $\mathbf{M}_{(hs)} \leftarrow \mathbf{E}_{(hs)}\mathbf{I}_{(hs)} \otimes \mathbf{1}_{(hs)}$ ▷ Matched filter in HS arm.

6:   $\boldsymbol{\Xi}_{(ms)} \leftarrow \mathbf{Adaptive\ coding}(\mathbf{M}_{(ms)}, \boldsymbol{\Gamma}_{(ms)})$ ▷ Computes the position for each class solving (15).

7:   $\boldsymbol{\Xi}_{(hs)} \leftarrow \mathbf{Adaptive\ coding}(\mathbf{M}_{(hs)}, \boldsymbol{\Gamma}_{(hs)})$ ▷ Computes the position for each class solving (17).

8:   $[\overline{\mathbf{Y}}^1_{(ms)} \ldots \overline{\mathbf{Y}}^{W-1}_{(ms)}] \leftarrow$ MULTISPECTRAL-ARM$\boldsymbol{\Gamma}_{(ms)}, \boldsymbol{\Xi}_{(ms)}$

9:   $[\overline{\mathbf{Y}}^0_{I(hs)} \ldots \overline{\mathbf{Y}}^{K-1}_{I(hs)}] \leftarrow$ HYPERSPECTRAL-ARM $\boldsymbol{\Gamma}_{(hs)}, \boldsymbol{\Xi}_{(hs)}$

10:   $\mathbf{R} \leftarrow [\text{vec}(\overline{\mathbf{Y}}^0_{(ms)}), \ldots, \text{vec}(\overline{\mathbf{Y}}^{W-1}_{(ms)}), \text{vec}(\overline{\mathbf{Y}}^0_{I(hs)}), \ldots, \text{vec}(\overline{\mathbf{Y}}^{K-1}_{I(hs)})]^T$ ▷ Spatio-spectral feature extraction.

11:   $\mathbf{C}_{training} \leftarrow \mathbf{SVM}_{training}(\mathbf{R})$ ▷ Classification labels using training data.

12:   $\mathbf{C}_{test} \leftarrow \mathbf{SVM}_{test}(\mathbf{R})$ ▷ Classification labels using test data.

13:   **return** $\mathbf{C}_{test}$ ▷ Output of the algorithm.

$\boldsymbol{\Gamma}_{(ms)} \in \{0, \gamma - 1\}^{M \times N}$ provides the prior spatial contextual information to the algorithm. The quantization matrix in the hyperspectral arm $\boldsymbol{\Gamma}_{(hs)} \in \{0, \gamma - 1\}^{\frac{M}{p} \times \frac{N}{p}}$ that is $\frac{1}{p}$ times the size compressive measurements $\mathbf{Y}_{(ms)}$.

B. Matched Filter

Once it is computed the contextual spatial information; the coded apertures are designed using the matched filter. The matched filter is computed by $\mathbf{M} = \mathbf{EB}$, where $\mathbf{E}$ is the average of the training samples of each class, and $\mathbf{B}$ are the designed complementary filters. The complementary filters are a set of filters that adds to an all-pass filter, avoiding the spectral redundancy of compressive measurements. The matched filter computes the spectral response between the designed complementary filters and the average training samples of each class.

1) Matched Filter in the Multispectral Arm: In particular, the matched filter in the multispectral arm is defined as $\mathbf{M}_{(ms)} = \mathbf{E}_{(ms)}\mathbf{B}_{(ms)}$, such that $\mathbf{M} \in \mathbb{R}^{\gamma \times n_{(ms)}}$, where it is assumed that $\gamma = n_c$, and the number of filters $n_{(ms)} = W$, with W the number of snapshots in the multispectral arm. Notice that $\mathbf{E}_{(ms)} \in \mathbb{R}^{\gamma \times \frac{L}{q}}$, where $\frac{L}{q}$ is the number of bands in the multispectral arm, and each column in $\mathbf{E}_{(ms)} = [\mathbf{e}_{(ms):,0}, \mathbf{e}_{(ms):,1}, \ldots, \mathbf{e}_{(ms):,\gamma-1}]^T$ is the average of the training samples for each of the classes. In addition, the matrix $\mathbf{B}_{(ms)} \in \{0,1\}^{\frac{L}{q} \times n_{f(ms)}}$ are the designed filters such that $\mathbf{B}_{(ms)} = [\mathbf{b}_{(ms):,0}, \mathbf{b}_{(ms):,1}, \ldots, \mathbf{b}_{(ms):,n_f-1}]$, where each column in $\mathbf{B}_{(ms)}$ is a part of the complementary filter with filter's width $\alpha_{(ms)} = \frac{L}{qW}$. The effect of a complementary filter is sampled a different part of the spectral signature at each snapshot. The designed filter is $\mathbf{B}_{(ms)} = \mathbf{I}_{(ms)} \otimes \mathbf{1}_{(ms)}$ where $\mathbf{1}_{(ms)}$ is all-ones vector such that $\mathbf{1}_{(ms)} \in \mathbb{R}^{\alpha_{(ms)} \times 1}$, $\mathbf{I}_{(ms)} \in \mathbb{R}^{W \times W}$ is the identity matrix, and $\otimes$ is the Kronecker product.

2) Matched Filter in the Hyperspectral Arm: The matched filter in the hyperspectral arm is denoted as $\mathbf{M}_{(hs)} = \mathbf{E}_{(hs)}\mathbf{B}_{(hs)}$,

such that $\mathbf{M}_{(hs)} \in \mathbb{R}^{\gamma \times n_{(hs)}}$, where it is assumed that $\gamma = n_c$, and the number of filters $n_{(hs)} = K$, with K the number of snapshots in the hyperspectral arm. Notice that $\mathbf{E}_{(hs)} \in \mathbb{R}^{\gamma \times L}$, where L is the number of bands in the hyperspectral arm, and each column in $\mathbf{E}_{(hs)} = [\mathbf{e}_{(hs):,0}, \mathbf{e}_{(hs):,1}, \ldots, \mathbf{e}_{(hs):,\gamma-1}]^T$ is the average of the training samples for each of the classes. Moreover, the matrix $\mathbf{B}_{(hs)} \in \{0,1\}^{L \times n_{f(hs)}}$ is the designed filter such that $\mathbf{B}_{(hs)} = [\mathbf{b}_{(hs):,0}, \mathbf{b}_{(hs):,1}, \ldots, \mathbf{b}_{(hs):,n_{f(hs)}-1}]$, where each column in $\mathbf{B}_{(hs)}$ is a complementary filter with filter's width $\alpha_{(hs)} = \frac{L}{K}$, which means that at each snapshot is capture a different wavelength. The designed filter is $\mathbf{B}_{(hs)} = \mathbf{I}_{(hs)} \otimes \mathbf{1}_{(hs)}$ where $\mathbf{1}_{(hs)}$ is all-ones vector such that $\mathbf{1}_{(hs)} \in \mathbb{R}^{\alpha_{(hs)} \times 1}$, $\mathbf{I}_{(hs)} \in \mathbb{R}^{K \times K}$ is the identity matrix, and $\otimes$ is the Kronecker product. In the successive stage, the adaptive coding is performed from the previous matched filter.

C. Adaptive Coded Aperture Design

To adaptive design the coded aperture entries, a sorting process is performed over the filter to determine the order of sampling according to the best spectral response [see (15) and (17)].

1) Adaptive Coding in the Multispectral Arm: To design the coded aperture is necessary to know the position of the filters at each snapshot, which can be computed as follows:

$$\boldsymbol{\Xi}_{(ms)(:,\boldsymbol{\Gamma}_{(ms)i,j})} = \text{sort}(\mathbf{M}^T_{(ms)(:,\boldsymbol{\Gamma}_{(ms)i,j})}) \qquad (15)$$

where sort(.) returns the sorted positions in descending order of the filters at each class. Notice that $\boldsymbol{\Xi}_{(ms)} \in \{0, \ldots, W - 1\}^{W \times \gamma}$ and the index of the filter is denoted by $\boldsymbol{\Xi}_{(ms)k,\boldsymbol{\Gamma}_{(ms_{i,j})}}$, where k indexes the snapshots and $\boldsymbol{\Gamma}_{(ms)_{i,j}}$ is the quantization matrix that index of the classes for each entry. The design of the coded aperture in the multispectral arm is giving by

$$\mathcal{T}^{(ms)}_{i,j,:,k} = \mathbf{b}_{(ms):,\boldsymbol{\Xi}_{(ms)k,\boldsymbol{\Gamma}_{(ms)(i,j)}}} \qquad (16)$$
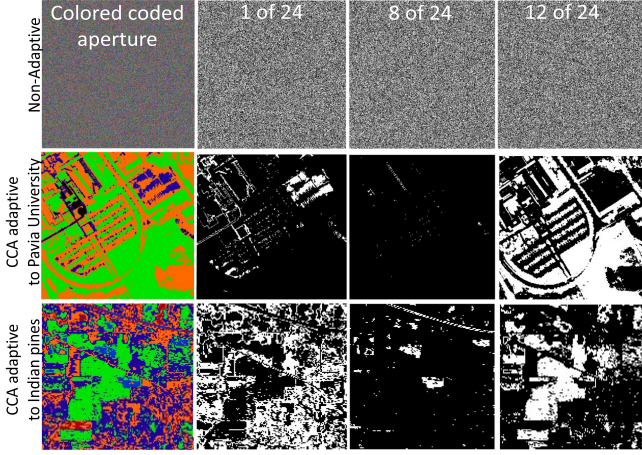
Fig. 3. Comparison between nonadaptive and adaptive colored coded apertures when $W = 6$. The top row shows the non-adaptive random colored coded aperture. The second and third rows depict the adaptive colored coded apertures for the Pavia University and Indian Pines, respectively. Notice the high correlation of the designed codes with the corresponding scene. (First column) Denote the false color representation of the colored coded apertures; (second column) show three slides of the 3-D block-unblock representation.

where $\mathbf{b}_{(\mathrm{ms}):,v}$ is the each designed filter in the vth class. Notice that the designed coded aperture in the ℓth spectral band for the wth multispectral snapshot can be reorganize as follows $\mathbf{T}_{(\mathrm{ms})}^{(w,\ell)} = \mathrm{diag}(\boldsymbol{\mathcal{T}}_{:,:,\ell,w}^{(\mathrm{ms})})$. In particular, the $\frac{L}{q}$ coded apertures in $\mathbf{T}_{(\mathrm{ms})}^w$ for the wth snapshot are rearranged to yield the sensing matrices $\overline{\mathbf{H}}_{(\mathrm{ms})}^w$ according to (9). The random and designed colored coded apertures are depicted in Fig. 3.

2) Adaptive Coding in the Hyperspectral Arm: In the same manner, the design of the coded apertures for the hyperspectral arm requires the location of the filters at each snapshot, which is denoted by

$$\boldsymbol{\Xi}_{(\mathrm{hs})(:,j)} = \mathrm{sort}(\mathbf{M}_{(\mathrm{hs})(:,\boldsymbol{\Gamma}_{(\mathrm{hs})i,j})}^T) \qquad (17)$$

where sort(.) returns the sorted positions in descending order of the filters at each class, the matrix is $\boldsymbol{\Xi}_{(\mathrm{hs})} \in \{0, \ldots, K - 1\}^{K \times \gamma}$, and the quantization matrix in the hyperspectral arm $\boldsymbol{\Gamma}_{(\mathrm{hs})}$. The index of each filter is denoted by $\boldsymbol{\Xi}_{(\mathrm{hs})k,\boldsymbol{\Gamma}_{(\mathrm{hs})i,j}}$, where k is the index of hyperspectral snapshots and $\boldsymbol{\Gamma}_{(\mathrm{hs})i,j}$ is the quantization matrix that index of the classes. The design of the coded aperture in the hyperspectral arm is giving by

$$\boldsymbol{\mathcal{T}}_{i,j,:,k}^{(\mathrm{hs})} = \mathbf{b}_{(\mathrm{hs}):,\boldsymbol{\Xi}_{(\mathrm{hs})k,\boldsymbol{\Gamma}_{(\mathrm{hs})i,j}}} \qquad (18)$$

where $\mathbf{b}_{(\mathrm{hs}):,v}$ is each designed filter in the vth class. Notice that the coded aperture in the ℓth band for the kth hyperspectral snapshot is rearranged as $\mathbf{T}_{(\mathrm{hs})}^{(k,\ell)} = \mathrm{diag}(\boldsymbol{\mathcal{T}}_{:,:,\ell,k}^{(\mathrm{hs})})$. In detail, the L coded apertures in $\mathbf{T}_{(\mathrm{hs})}^k$ for the kth snapshot can be rearranged as the sensing matrix $\overline{\mathbf{H}}_{(\mathrm{hs})}^k$ using (11). Once, the coded are designed the compressive measurements are captured.
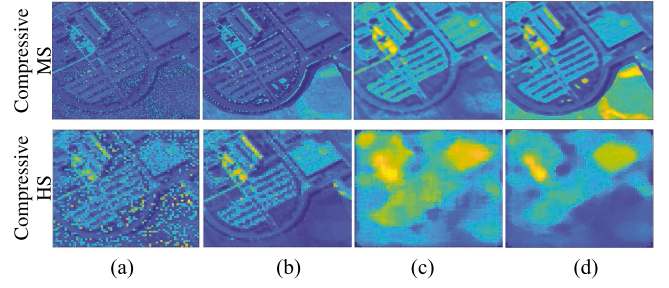

Fig. 4. Denoising of compressive measurements. (a) Multispectral compressive measurements using nonadaptive coded apertures. (b) Hyperspectral compressive measurements using nonadaptive coded apertures. (c) Multispectral compressive measurements using adaptive coded apertures. (d) Hyperspectral compressive measurements using adaptive coded apertures. Compressive measurements after median filter with window size $[7 \times 7]$, using nonadaptive coded apertures (e), and (f), using adaptive coded apertures (g) and (h).

D. Acquisition of Compressive Measurements

In the fourth stage, each arm captures a different type of compressive measurement. At each snapshot, the multispectral compressive measurements $\mathbf{y}_{(\mathrm{hs})}^k = \overline{\mathbf{H}}_{(\mathrm{hs})}^k \mathbf{D}_{(\mathrm{hs})} \mathbf{f} + \boldsymbol{\eta}_{(\mathrm{hs})}^k$ are captured, and the hyperspectral compressive measurements $\mathbf{y}_{(\mathrm{ms})}^w = \overline{\mathbf{H}}_{(\mathrm{ms})}^w \mathbf{D}_{(\mathrm{ms})} \mathbf{f} + \eta_{(\mathrm{ms})}^w$ are captured. Fig. 4 depicts an example of the compressive measurements of the multispectral and hyperspectral arms. Notice that when the coded apertures are spatially and spectrally complementary but randomly distributed, a salt and pepper noise is produced over the compressive measurements [see Fig. 4(a), and 4(b)]. In contrast, when the coded apertures are designed the salt pepper noise is prevented [see Fig. 4(c), and 4(d)]. Nevertheless, in order to include the spatial contextual information in the extracted features, a denoising stage is required. The following subsection explains the denoising method, and the extraction of features.

E. Denoising and Feature Extraction

In the denoising stage, a median filter is applied over the compressive multispectral, and hyperspectral measurements $Y_{i,j,k}^{(hs)}$, and $Y_{i,j,w}^{(ms)}$ to enhance the spatial contextual information. To compute the output of the median filter, an odd number of samples are sorted, and the middle value is used as the output of the filter. If the filter length is $\iota = 2\beta + 1$, the filtering procedure is denoted as $\overline{Y}_{i,j,k}^{(hs)} = \mathbf{MED}[Y_{i,j-\beta,k}^{(hs)}, \ldots, Y_{i,j,k}^{(hs)} \ldots Y_{i,j+\beta,k}^{(hs)}]$, and $\overline{Y}_{i,j,k}^{(ms)} = \mathbf{MED}[Y_{i,j-\beta,w}^{(ms)}, \ldots, Y_{i,j,w}^{(ms)}, \ldots Y_{i,j+\beta,k}^{(hs)}]$, where $\overline{Y}_{i,j,w}^{(ms)}$, and $\overline{Y}_{i,j,k}^{(hs)}$ are the (i,j)th multispectral, and hyperspectral output, respectively. The median filter with window's size $[7 \times 7]$ is performed to promote the uniformity in both compressive measurements $Y_{i,j,k}^{(hs)}, Y_{i,j,w}^{(ms)}$.

In addition, the filtered hyperspectral measurements $\overline{\mathbf{Y}}_{(\mathrm{hs})}^k$ are interpolated using a bilinear interpolator $\mathbf{P}$ to attain the size of the multispectral measurements, resulting in $\overline{\mathbf{Y}}_{\mathrm{I}(\mathrm{hs})}^k = \mathbf{P}(\overline{\mathbf{Y}}_{(\mathrm{hs})}^k)$. Using the filtered compressive multispectral measurements $\overline{\mathbf{Y}}_{(\mathrm{ms})}^w$, and the filtered-interpolated compressive hyperspectral measurements

Algorithm 2: Adaptive Coding and Processing in the Hyperspectral-Arm.

function HYPERSPECTRAL-ARM$\mathbf{\Gamma}_{(hs)}, \mathbf{\Xi}_{(ms)}$
2:      **for** $k \leftarrow 0, K-1$ **do**
         for $i \leftarrow 0, \frac{M}{p}$ **do**
4:          **for** $j \leftarrow 0, \frac{N}{p}$ **do**
             $v \leftarrow \mathbf{\Xi}_{(hs)k}, \mathbf{\Gamma}_{(hs)(i,j)}$
6:              $\mathcal{T}_{i,j,:,k}^{(hs)} \leftarrow \mathbf{b}_{(hs):,v}$
             $\mathbf{Y}_{(hs)}^k \leftarrow \mathbf{Acq}(\mathcal{T}_{i,j,:,k}^{(hs)})$ ▷ Hyperspectral measurements acquisition using (6).
8:              $\overline{\mathbf{Y}}_{(hs)}^k \leftarrow \mathbf{Med}(\mathbf{Y}_{(hs)}^k)$ ▷ Compute median filtering.
             $\overline{\mathbf{Y}}_{I(hs)}^k \leftarrow \mathbf{P}(\overline{\mathbf{Y}}_{(hs)}^k)$ ▷ Interpolation of hyperspectral measurements.
10:      **return** $[\overline{\mathbf{Y}}_{I(hs)}^1 \ldots \overline{\mathbf{Y}}_{I(hs)}^{K-1}]$

Algorithm 3: Adaptive Coding and Processing in the Multispectral-Arm.

function MULTISPECTRAL-ARM$\mathbf{\Gamma}_{(ms)}, \mathbf{\Xi}_{(ms)}$
2:      **for** $w \leftarrow 1, W-1$ **do**
         for $i \leftarrow 0, M$ **do**
4:          **for** $j \leftarrow 0, N$ **do**
             $v \leftarrow \mathbf{\Xi}_{(ms)w}, \mathbf{\Gamma}_{(ms)(i,j)}$
6:              $\mathcal{T}_{i,j,:,w}^{(ms)} \leftarrow \mathbf{b}_{(ms):,v}$
             $\mathbf{Y}_{(ms)}^w \leftarrow \mathbf{Acq}(\mathcal{T}_{i,j,:,w}^{(ms)})$ ▷ Acquisition of multispectral measurements using (6).
8:              $\overline{\mathbf{Y}}_{(ms)}^w \leftarrow \mathbf{Med}(\mathbf{Y}_{(ms)}^w)$ ▷ Compute median filtering.
     return $[\overline{\mathbf{Y}}_{(ms)}^0 \ldots \overline{\mathbf{Y}}_{(ms)}^{W-1}]$

$\overline{\mathbf{Y}}_{I(hs)}^k$, the features are extracted in the matrix $\mathbf{R} = [\text{vec}(\overline{\mathbf{Y}}_{(ms)}^0), \ldots, \text{vec}(\overline{\mathbf{Y}}_{(ms)}^{W-1}), \text{vec}(\overline{\mathbf{Y}}_{I(hs)}^0), \ldots, \text{vec}(\overline{\mathbf{Y}}_{I(hs)}^{K-1})]^T$. Fig. 4(e) and (f) depicts the spatial and spectral features after applying the median filter to the nonadaptive compressive measurements. In contrast, Fig. 4(g) and (h) shows the spatial $\overline{\mathbf{Y}}_{(ms)}^w$, and spectral $\overline{\mathbf{Y}}_{I(hs)}^k$ features after applying the median filter to the adaptive compressive measurements. Notice that compressive measurements using the nonadaptive approach attain lower spatial uniformity Fig. 4(e) and (f) than the compressive measurements obtained using the proposed adaptive design.

F. Classification

The classification is performed using as input the extracted features of the previous step. The SVM classifier [4], using a polynomial kernel computes the class labels for training $\mathbf{C}_{training}$, and the class labels for test $\mathbf{C}_{test}$ to each spatial position of the scene.

G. Algorithm

The algorithm 1 summarizes the proposed method. Which has as input the compressive measurement of the multispectral arm $\mathbf{Y}_{(ms)}^0$. Using the $\mathbf{Y}_{(ms)}^0$, the high-pass filter is calculated in step 4. Following, the quantization is computed in step 5. Subsequently, the compressive measurements are captured $\mathbf{Y}_{(ms)}^w$, $\mathbf{Y}_{(hs)}^k$, according to the sampling model in lines 10 and 11. The process to obtain $\mathbf{Y}_{(ms)}^w$, and $\mathbf{Y}_{(hs)}^k$ is shown in algorithms 2 and 3. In the adapting coding process, the sampling matrix is designed using the contextual information of the quantization matrix $\mathbf{\Gamma}$. The coded apertures $\mathcal{T}_{i,j,:,k}^{(hs)}$, and $\mathcal{T}_{i,j,:,k}^{(ms)}$ are computed in lines 6 of algorithms 2 and 3, respectively. The acquisition of the hyperspectral and multispectral compressive measurements using the adapted codes is attained in lines 7, and 7 of algorithms 2 and 3. The processing before to attain the features is composed of denoising, and the interpolation. The denoising using median
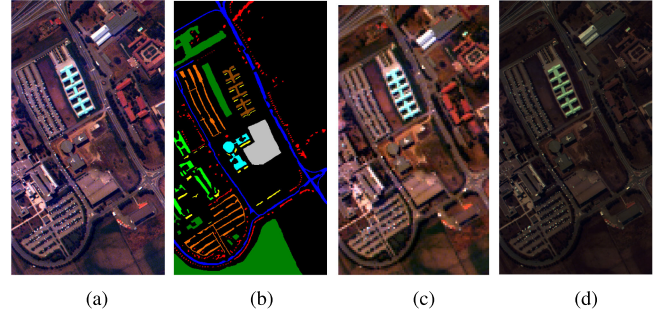

Fig. 5. Pavia University dataset. (a) RGB version of the high-resolution image, (b) ground truth map, (c) RGB version of the HS image, (d) RGB version of the MS image.

filter is conducted in line 8 of algorithms 2, and 3, respectively. And, the interpolation is only performed to hyperspectral measurements in line 9 of algorithm 2. Retaking the algorithm 1, the extracted features denoted as matrix $\mathbf{R}$ are computed in line 12. After, the classification is computed in lines 13 and 14. The output of the algorithm is the resulting classification labels $\mathbf{C}_{test}$.

IV. SIMULATIONS AND RESULTS

This section analyzes the performance of the proposed adaptive technique in terms of spectral image classification accuracy. More precisely, the proposed method is evaluated on synthetic compressive measurements obtained from two real datasets: Pavia University and Indian Pines. Subsequently, the proposed approach is tested on real compressive measurements captured by a laboratory setup.

A. Pavia University Dataset

The first spectral image was obtained by the reflective optics imaging spectrometer (ROSIS-02) over an urban region surrounding the campus of the University of Pavia, Italy [36]. This spectral image exhibits dimensions of 640×340 pixels and 96 spectral reflectance bands in the wavelength interval from 0.43 to 0.86 μm. A RGB composite of the Pavia University dataset is shown in Fig. 5(a). Furthermore, the ground truth labeling map

TABLE I
PERFORMANCE OF THE PROPOSED ADAPTIVE METHOD ON THE PAVIA
UNIVERSITY DATASET FOR DIFFERENT SIZES OF THE MEDIAN FILTER

System	Metric	Windows size				
		3×3	5×5	7×7	9×9	11×11
3D-CASSI	OA(%)	94.77	95.33	96.24	96.96	97.56
	AA(%)	92.98	93.94	94.86	95.35	95.72
	κ	0.931	0.938	0.950	0.960	0.968
C-CASSI	OA(%)	86.25	89.45	91.58	92.97	94.04
	AA(%)	78.84	83.12	86.18	88.18	89.82
	κ	0.816	0.859	0.888	0.906	0.921

with $n_c = \gamma = 9$ is illustrated in Fig. 5(b), where every label refers to a distinct structure in a urban cover.

To evaluate the performance of the proposed method, the compressive measurements are obtained using the proposed adaptive acquisition approach. To this end, the low-spectral resolution HS image is obtained by downsampling the high-resolution spectral image with a spatial decimation factor $p = 4$. Therefore, the HS image consists of 160×85 pixels and 96 spectral bands. The RGB version of the HS image is shown in Fig. 5(c). On the other hand, the low-spectral resolution MS image is obtained by downsampling the high-resolution image with a spectral decimation factor $q = 4$. Hence, the MS image exhibits a size of $640 \times 340 \times 24$. Fig. 5(d) displays the RGB version of the MS image.

Subsequently, we implement the proposed adaptive method by simulating the dual-arm acquisition system. In this work, we simulate two dual-arm systems. Notice that each dual-arm system is equipped with two CSI sensors belonging to a particular optical architecture: 3-D-CASSI [20] or C-CASSI [23]. To label the spectral image, a supervised pixel-based classifier is applied to the extracted features. More precisely, we use SVM with a polynomial kernel of degree $d = 3$.

We evaluate the effectiveness of the proposed classification approach for different parameter settings. In particular, Table I shows the accuracy results obtained by the proposed approach for different window sizes of the median filter. Specifically, we display the ensemble average of the overall accuracy (OA), the average accuracy (AA), and the Cohen's kappa statistic (κ) for distinct sizes of the median filter. For this experiment, the compression ratio is fixed to $\rho = 16.67\%$. Each value is the ensemble average of 25 realizations and at each trial, a different set of training samples is randomly selected from the ground truth map. Unless stated otherwise, 10% of the image pixels are randomly selected as training samples and the remaining pixels are considered as test samples. As can be observed in Table I, the performance of the proposed approach improves as the window size increases.

Fig. 6 shows the classification maps obtained by the proposed adaptive approach using a dual-arm system with 3-D-CASSI sensors for different compression ratios. Note that the compression ratio of 3-D-CASSI and C-CASSI are given by

$$\rho = K \left(\frac{M(N + cL - c)}{p^2 MNL} \right) + W \left(\frac{M(N + \frac{cL}{p} - c)}{MNL} \right) \quad (19)$$
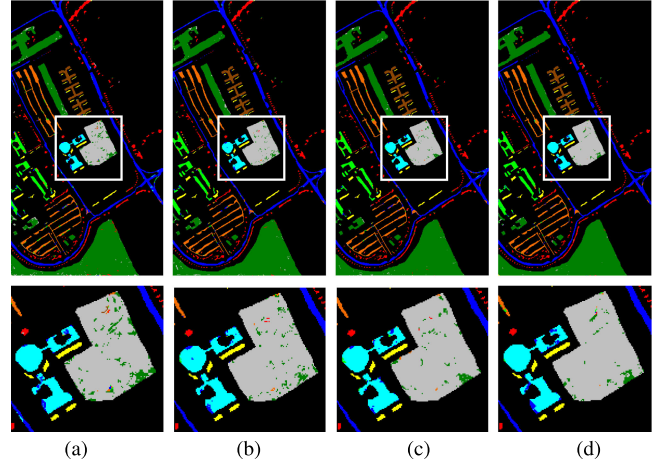

Fig. 6. Pavia University dataset. Labeling maps from adaptive 3-D-CASSI measurements for (a) $\rho = 8.33\%$ with OA: 94.37%, (b) $\rho = 12.50\%$ with OA: 95.92%, (c) $\rho = 16.67\%$ with OA: 96.52%, and (d) $\rho = 25.00\%$ with OA: 97.19%.
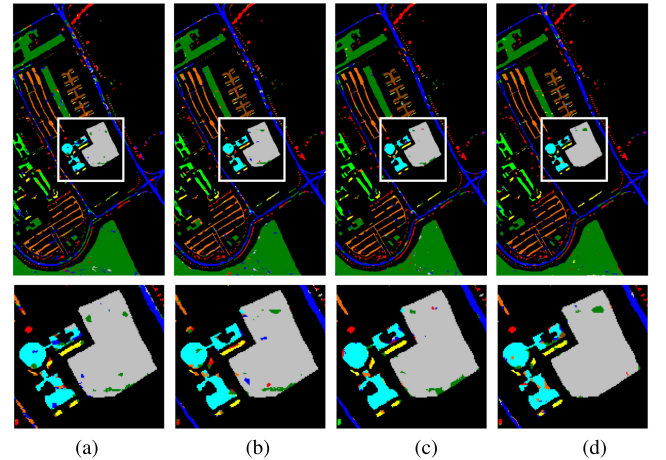

Fig. 7. Pavia University dataset. Labeling maps from adaptive C-CASSI measurements for (a) $\rho = 8.33\%$ with OA: 84.82%, (b) $\rho = 12.50\%$ with OA: 89.40%, (c) $\rho = 16.67\%$ with OA: 91.27%, and (d) $\rho = 25.00\%$ with OA: 91.18%.

where c is a parameter related to the spectral shifting of the encoded image, K and W denote the number of camera shots captured by the hyperspectral and multispectral arm, respectively. In addition, we set the window size of the median filter to 7×7. Fig. 7 illustrates the labeling maps using the dual-arm system with C-CASSI sensors for different compression ratios.

To test the performance of the proposed adaptive approach for different detector resolutions, Table II shows the labeling accuracy for various downsampling factors. Specifically, each value is obtained by averaging 25 realizations of the respective experiment. Notice that the window size of the median filter is fixed to $[7 \times 7]$ and the compression ratio is set to $\rho = 16.67\%$. Moreover, the results are obtained using 3-D-CASSI and C-CASSI architectures. The ensemble average of OA, AA, and κ are also shown in the three last rows of Table II, where the best values of OA, AA, and κ are shown in bold font for each

TABLE II
PERFORMANCE OF THE PROPOSED ADAPTIVE METHOD ON THE PAVIA
UNIVERSITY DATASET FOR DIFFERENT SENSOR RESOLUTIONS

|		3D-CASSI				C-CASSI			
		$p=2$		$p=4$		$p=2$		$p=4$	
Color	Class	$q=2$	$q=4$	$q=2$	$q=4$	$q=2$	$q=4$	$q=2$	$q=4$
	Asphalt	97.90	97.63	97.57	97.18	95.52	84.56	95.91	86.45
	Meadows	98.90	98.77	98.65	98.20	98.81	96.20	98.58	97.20
	Gravel	94.23	93.23	91.65	90.62	90.83	64.03	93.22	81.78
	Trees	96.22	95.31	95.49	93.04	83.58	75.81	80.51	74.88
	Metal	98.83	99.09	98.19	98.28	97.73	93.04	95.93	92.19
	Soil	95.77	95.49	94.87	93.88	99.04	98.04	98.52	97.03
	Bitumen	96.31	95.78	94.28	92.11	94.01	91.45	93.42	89.07
	Bricks	97.31	97.19	94.96	94.00	94.25	89.82	96.95	91.07
	Shadows	98.00	97.18	97.52	96.18	79.53	70.76	73.59	67.15
OA (%)		**97.72**	97.43	96.98	96.20	**95.84**	90.22	95.67	91.55
AA (%)		**97.05**	96.63	95.91	94.83	**92.59**	84.86	91.85	86.31
κ		**0.970**	0.966	0.960	0.950	**0.945**	0.869	0.942	0.887
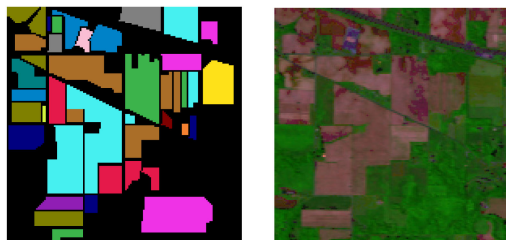
Fig. 8. Indian Pines dataset. (left) RGB composite of the high-resolution spectral image, and (right) ground truth map.

optical architecture. As can be observed in this table, the best classification performance is obtained when ($p=2$, $q=2$).

B. Indian Pines Dataset

This spectral image was acquired by the airborne visible, infrared imaging spectrometer (AVIRIS) over the Indian Pines, USA [36]. This dataset consists of is 145×145 pixels and 192 spectral bands in the wavelength interval from 0.5 to 2.5 μm. An RGB composite of the high-resolution spectral image is illustrated in Fig. 8(left). Furthermore, Fig. 8(right) shows the ground truth map with $n_c = \gamma = 16$ different classes that identify different crops and building structures.

1) 3-D-CASSI: Fig. 9 displays the labeling maps obtained by the proposed adaptive approach using a dual-arm system with 3-D-CASSI sensors. For comparison purposes, we also show the classification maps obtained by the nonadaptive approach reported in [37]. For this dataset, we set $\rho = 16.67\%$ and the window size of the median filter is fixed to $[9 \times 9]$. The nonadaptive approach generates degraded labeling maps with low OA values 49.89%, 56.55%, 59.73%, and 64.83% in comparison to those obtained using the adaptive approach 85.55%, 86.27%, 87.47%, and 87.70% for different compression ratios. The proposed approach attains 85.55% of OA in classification using 2 multispectral shots and 8 hyperspectral shots. In contrast, the nonadaptive approach obtains 49.89% for the same number of snapshots. Hence, the proposed adaptive method exhibits an accuracy gain of at least 20% compared to that obtained by the nonadaptive approach.

2) C-CASSI: Fig. 10 depicts the labeling maps using a dual-arm system with C-CASSI sensors. The nonadaptive approach
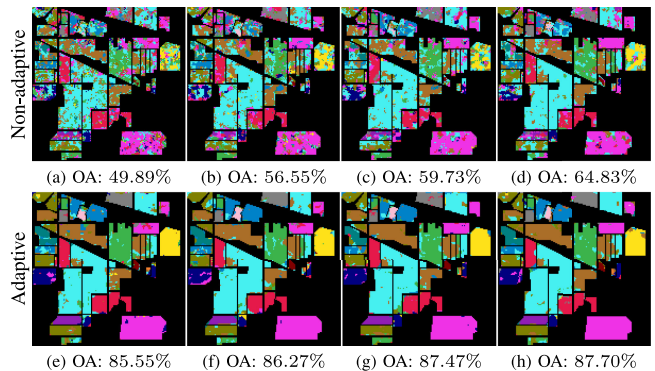

Fig. 9. Indian Pines dataset. Labeling maps using 3-D-CASSI systems for different compression ratios. Nonadaptive approach with (a) $\rho = 8.33\%$, (b) $\rho = 12.50\%$, (c) $\rho = 16.67\%$, (d) $\rho = 25.00\%$. Proposed adaptive approach with (e) $\rho = 8.33\%$, (f) $\rho = 12.50\%$, (g) $\rho = 16.67\%$, and (h) $\rho = 25.00\%$.
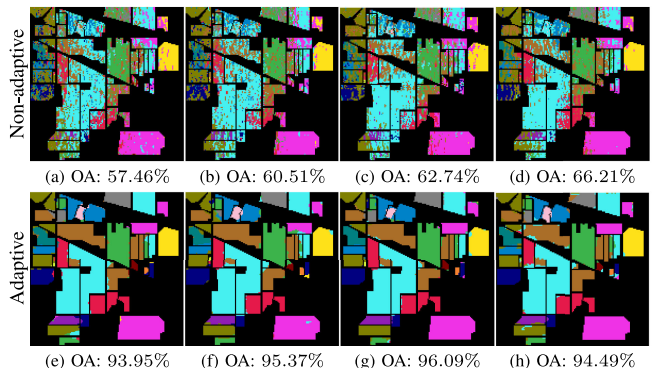

Fig. 10. Indian Pines dataset. Labeling maps using C-CASSI systems for different compression ratios. Nonadaptive approach with (a) $\rho = 8.33\%$, (b) $\rho = 12.50\%$, (c) $\rho = 16.67\%$, (d) $\rho = 25.00\%$. Proposed adaptive approach with (e) $\rho = 8.33\%$, (f) $\rho = 12.50\%$, (g) $\rho = 16.67\%$, and (h) $\rho = 25.00\%$.
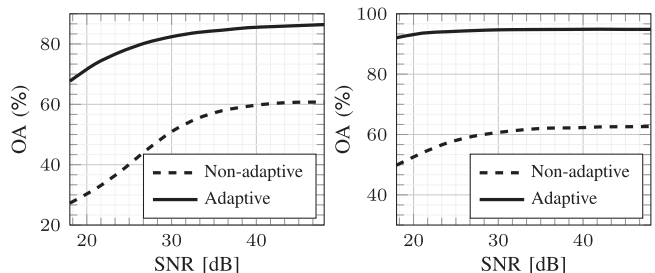

Fig. 11. Indian Pines dataset. OA versus the SNR of the compressive samples for (left) 3-D-CASSI and (right) C-CASSI.

achieves low OA values 57.46%, 60.51%, 62.74%, and 66.21% compared to the results obtained utilizing the adaptive approach 93.95%, 95.37%, 96.09%, and 94.49%.

To observe the performance of the proposed approach against the variability caused by sensor noise [38], Fig. 11 shows the OA as the SNR of the camera projections increases for 3-D-CASSI and C-CASSI. In this case, we assume that projections are contaminated by noise matrices whose entries are iid random

TABLE III
COMPUTATION TIMES IN SECONDS ON THE INDIAN PINES DATASET FOR DIFFERENT COMPRESSION RATIOS

System	Method	Compression ratios (ρ)			
		8.33%	12.50%	16.67%	25.00%
3D-CASSI	Non-adaptive	0.0708	0.1157	0.1528	0.2262
	Adaptive	0.1734	0.2579	0.3349	0.4857
C-CASSI	Non-adaptive	0.1013	0.1613	0.2155	0.3201
	Adaptive	0.2287	0.3389	0.4417	0.6393

samples following a Gaussian distribution. For comparison purposes, we also show the OA curve yielded by the nonadaptive approach. Each point of the curve is the ensemble average of 100 realizations. For each trial, a different set of contamination matrices is generated and a different training set is selected. As can be seen in this figure, the proposed approach exhibits outstanding performance compared to the nonadaptive approach. Finally, Table III displays the execution times generated by the methods under test. For this experiment, the computation times are obtained using a desktop with an Intel Core i7 CPU, 3.00 GHz, 64-GB RAM, and Ubuntu 18.04 operating system. Although the proposed approach is slower than the nonadaptive method, the computation times are competitive with a remarkable accuracy gain.

C. Experiments With Real Data

To experimentally prove the benefit of the proposed classification approach the dual-arm C-CASSI was used to acquire compressive measurements in the multispectral and hyperspectral in accordance with [24]. In the following repository is available the ground truth, the datacube and the source code.[1] The apparatus is made up of an objective lens (Thorlabs, MAP10100100-A) and a DMD (Texas Instruments, DLI4130VIS-7XGA) to encode the spectral image. The optical setup is composed of two arms. The multispectral arm employs a relay lens (Thorlabs, MAP10100100-A), a dual Amici prism (Shanghai Optics, custom made), and a monochrome sensor (AVT, Stingray F-080B) with 1032×776 pixels and pixel size of $4.65 \times 4.65 \mu$m. The hyperspectral arm utilizes a 4F-relay system build using two lenses (Thorlabs, AC254-100-A-ML), with a transmission diffraction grating (Thorlabs, GT50-03, 300 grooves/mm, 17.5 groove angle) in the middle, and a monochrome sensor (AVT, Stingray F-080B).

Hereinafter, the evaluation of the performance of the proposed classification approach is presented. One target scene, named Hen is used to evaluate the performance of the computational classification setup. In particular, Fig. 12 depicts the ground-truth and the RGB version of the scene using the testbed implementation. The test use measurements data of 3-D-CASSI, C-CASSI optical setup. A combination of multispectral and hyperspectral snapshots $w = \{2, 3, 4, 6\}$ and $k = \{8, 12, 16, 24\}$, respectively. The spatial resolution of the emulated dataset is 512×512, and spectral resolution is 96 bands, and $n_c = 4$.

[1]The ground truth, the datacube, and the source code can be downloaded from the following repository: https://github.com/nelson10/CompressiveAdaptiveClassificationMultisensor.
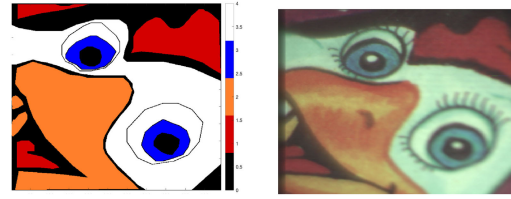

Fig. 12. Laboratory dataset. (left) Ground truth map of the scene with $n_c = 4$ classes, and (right) the RGB version of the scene.
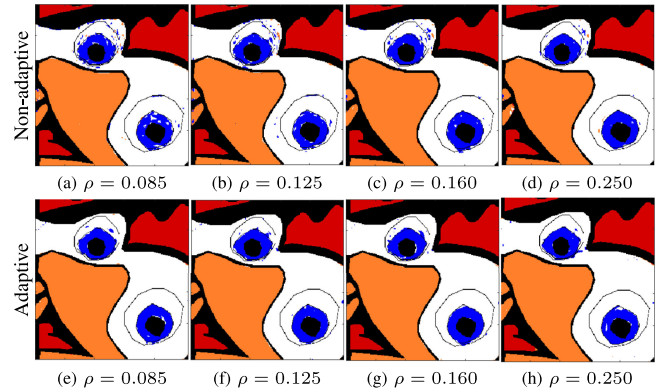

Fig. 13. Hen dataset. Labeling maps from 3-D-CASSI measurements. Nonadaptive approach (a) OA:97.76%, (b) OA:98.10%, (c) OA:98.67%, and (d) OA:99.11%. Proposed (e) OA:99.19%, (f) OA:99.24%, (g) OA:99.11%, and (h) OA:99.19%.
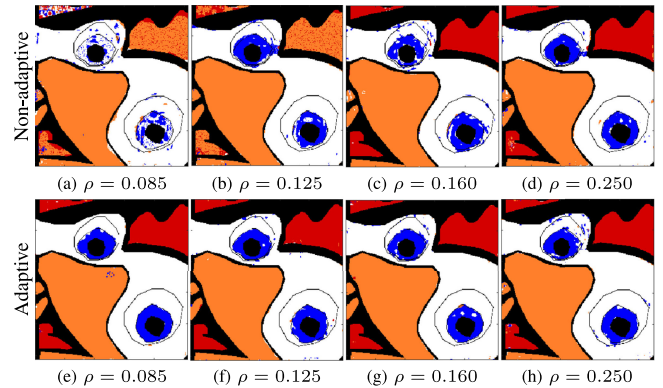

Fig. 14. Hen dataset. Labeling maps from C-CASSI measurements. Nonadaptive approach (a) OA:80.74%, (b) OA:84.35%, (c) OA:97.03%, (d) OA:97.90%. Proposed (e) OA:99.18%, (f) OA:98.60%, (g) OA:98.60%, and (h) OA:98.19%.

To compare Figs. 13 and 14 shown in the classification map obtained using the nonadaptive and adaptive approach the 3-D-CASSI and the adaptive C-CASSI. A significant improvement is shown when the compression ratio is $\rho = 0.085$, 1.43% for the 3-D-CASSI, and 18.44% C-CASSI.

V. CONCLUSION

A method that adaptively designs the coded apertures to classify multispectral and hyperspectral compressive measurements of spectral images has been developed. In detail, the approach captures a prior estimation of the grayscale image in the multispectral arm using a coded aperture with all entries

with a bandpass filter to reduce the dispersion of the measurement of the first snapshot. The discrete mathematical model to design adaptive colored-coded apertures of the dual-arm CSI is presented. The approach filter, and quantize the prior estimation of the grayscale image according to the number of classes. Moreover, the matched filter design the coded aperture by computing spectral response between the designed filters and the average training samples. The performance of the proposed classification approach is assessed on two spectral datasets under the OA metric. The simulation test also shows a remarkable improvement in the accuracy classification in up to 99.68% in the OA metric. According to the simulation results, a significant reduction in the number of snapshots in the hyperspectral and multispectral arm is achieved using the proposed approach. Notice that the approach is successfully implemented on real compressive measurements. The testbed implementation shows a significant improvement in the overall accuracy.

ACKNOWLEDGMENT

REFERENCES

[1] D. G. Goodenough *et al.*, "Processing hyperion and ali for forest classification," *IEEE Trans. Geosci. Remote Sens.*, vol. 41, no. 6, pp. 1321–1331, Jun. 2003.

[2] U. Amato *et al.*, "Statistical classification for assessing prisma hyperspectral potential for agricultural land use," *IEEE J. Sel. Topics Appl. Earth Observ. Remote Sens.*, vol. 6, no. 2, pp. 615–625, Apr. 2013.

[3] C. Yang, J. H. Everitt, Q. Du, B. Luo, and J. Chanussot, "Using high-resolution airborne and satellite imagery to assess crop growth and yield variability for precision agriculture," *Proc. IEEE Proc. IRE*, vol. 101, no. 3, pp. 582–592, Mar. 2013.

[4] F. Melgani and L. Bruzzone, "Classification of hyperspectral remote sensing images with support vector machines," *IEEE Trans. Geosci. Remote Sens.*, vol. 42, no. 8, pp. 1778–1790, Aug. 2004.

[5] S. R. Joelsson, J. A. Benediktsson, and J. R. Sveinsson, "Random forest classifiers for hyperspectral data," in *Proc. IEEE Int. Geosci. Remote Sens. Symp.*, 2005, vol. 1, pp. 4–pp, doi: 10.1109/IGARSS.2005.1526129.

[6] P. O. Gislason, J. A. Benediktsson, and J. R. Sveinsson, "Random forests for land cover classification," *Pattern Recognit. Lett.*, vol. 27, no. 4, pp. 294–300, 2006.

[7] F. Ratle, G. Camps-Valls, and J. Weston, "Semisupervised neural networks for efficient hyperspectral image classification," *IEEE Trans. Geosci. Remote Sens.*, vol. 48, no. 5, pp. 2271–2282, May 2010.

[8] Y. Chen, N. M. Nasrabadi, and T. D. Tran, "Hyperspectral image classification using dictionary-based sparse representation," *IEEE Trans. Geosci. Remote Sens.*, vol. 49, no. 10, pp. 3973–3985, Oct. 2011.

[9] J. Li, J. M. Bioucas-Dias, and A. Plaza, "Spectral-spatial hyperspectral image segmentation using subspace multinomial logistic regression and Markov random fields," *IEEE Trans. Geosci. Remote Sens.*, vol. 50, no. 3, pp. 809–823, Mar. 2012.

[10] G. Hughes, "On the mean accuracy of statistical pattern recognizers," *IEEE Trans. Inf. Theory*, vol. 14, no. 1, pp. 55–63, Jan. 1968.

[11] Z. Ye, H. Li, Y. Song, J. A. Benediktsson, and Y. Y. Tang, "Hyperspectral image classification using principal components-based smooth ordering and multiple 1-D interpolation," *IEEE Trans. Geosci. Remote Sens.*, vol. 55, no. 2, pp. 1199–1209, Feb. 2017.

[12] N. Falco, J. A. Benediktsson, and L. Bruzzone, "A study on the effectiveness of different independent component analysis algorithms for hyperspectral image classification," *IEEE J. Sel. Topics Appl. Earth Observ. Remote Sens.*, vol. 7, no. 6, pp. 2183–2199, Jun. 2014.

[13] G. Camps-Valls and L. Bruzzone, "Kernel-based methods for hyperspectral image classification," *IEEE Trans. Geosci. Remote Sens.*, vol. 43, no. 6, pp. 1351–1362, Jun. 2005.

[14] J. Arenas-Garcia, K. B. Petersen, G. Camps-Valls, and L. K. Hansen, "Kernel multivariate analysis framework for supervised subspace learning: A tutorial on linear and kernel multivariate methods," *IEEE Signal Process. Mag.*, vol. 30, no. 4, pp. 16–29, Jun. 2013.

[15] N. Falco, J. A. Benediktsson, and L. Bruzzone, "Spectral and spatial classification of hyperspectral images based on ICA and reduced morphological attribute profiles," *IEEE Trans. Geosci. Remote Sens.*, vol. 53, no. 11, pp. 6223–6240, Nov. 2015.

[16] M. Fauvel, Y. Tarabalka, J. A. Benediktsson, J. Chanussot, and J. C. Tilton, "Advances in spectral-spatial classification of hyperspectral images," *Proc. IEEE Proc. IRE*, vol. 101, no. 3, pp. 652–675, Mar. 2013.

[17] J. Zhao, Y. Zhong, H. Shu, and L. Zhang, "High-resolution image classification integrating spectral-spatial-location cues by conditional random fields," *IEEE Trans. Image Process.*, vol. 25, no. 9, pp. 4033–4045, Sep. 2016.

[18] B. Rasti *et al.*, "Feature extraction for hyperspectral imagery: The evolution from shallow to deep: Overview and toolbox," *IEEE Geosci. Remote Sens. Mag.*, vol. 8, no. 4, pp. 60–88, Dec. 2020.

[19] D. Hong, L. Gao, J. Yao, B. Zhang, A. Plaza, and J. Chanussot, "Graph convolutional networks for hyperspectral image classification," *IEEE Trans. Geosci. Remote Sens.*, vol. 59, no. 7, pp. 5966–5978, Jul. 2021.

[20] X. Cao *et al.*, "Computational snapshot multispectral cameras: Toward dynamic capture of the spectral world," *IEEE Signal Process. Mag.*, vol. 33, no. 5, pp. 95–108, Sep. 2016.

[21] A. Wagadarikar, R. John, R. Willett, and D. Brady, "Single disperser design for coded aperture snapshot spectral imaging," *Appl. Opt.*, vol. 47, no. 10, pp. B 44--B51, Apr. 2008.

[22] M. E. Gehm, R. John, D. J. Brady, R. M. Willett, and T. J. Schulz, "Single-shot compressive spectral imaging with a dual-disperser architecture," *Opt. Exp.*, vol. 15, no. 21, pp. 14013–14027, Oct. 2007.

[23] H. Arguello and G. R. Arce, "Colored coded aperture design by concentration of measure in compressive spectral imaging," *IEEE Trans. Image Process.*, vol. 23, no. 4, pp. 1896–1908, Apr. 2014.

[24] H. Rueda-Chacon, F. Rojas, D. R. Molina, and H. Arguello, "Demonstration of a compressive hyperspectral image fusion optical imager," in *Proc. Comput. Opt. Sens. Imag.*, 2020, Paper CW 4B–6.

[25] H. Rueda-Chacon, F. Rojas, D. R. Molina, and H. Arguello, "Compressive spectral fusion via a single aperture high throughput imaging system," *Sci. Rep.*, vol. 11, no. 1, pp. 1–12, 2021.

[26] A. Ramirez, H. Arguello, G. R. Arce, and B. M. Sadler, "Spectral image classification from optimal coded-aperture compressive measurements," *IEEE Trans. Geosci. Remote Sens.*, vol. 52, no. 6, pp. 3299–3309, Jun. 2014.

[27] M. Dunlop-Gray, P. Poon, D. Golish, E. Vera, and M. Gehm, "Experimental demonstration of an adaptive architecture for direct spectral imaging classification," *Opt. Exp.*, vol. 24, no. 16, pp. 18 307–18 321, Aug. 2016.

[28] D. Hong *et al.*, "More diverse means better: Multimodal deep learning meets remote-sensing imagery classification," *IEEE Trans. Geosci. Remote Sens.*, vol. 59, no. 5, pp. 4340–4354, May 2021.

[29] P. Ghamisi *et al.*, "Multisource and multitemporal data fusion in remote sensing: A comprehensive review of the state of the art," *IEEE Geosci. Remote Sens. Mag.*, vol. 7, no. 1, pp. 6–39, Mar. 2019.

[30] J. M. Ramirez and H. Arguello, "Multiresolution compressive feature fusion for spectral image classification," *IEEE Trans. Geosci. Remote Sens.*, vol. 57, no. 12, pp. 9900–9911, Dec. 2019.

[31] J. M. Ramirez and H. Arguello, "Spectral image classification from multisensor compressive measurements," *IEEE Trans. Geosci. Remote Sens.*, vol. 58, no. 1, pp. 626–636, Jan. 2020.

[32] J. M. Ramirez, J. I. Martínez Torre, and H. Arguello, "Feature fusion via dual-resolution compressive measurement matrix analysis for spectral image classification," *Signal Process.: Image Commun.*, vol. 90, 2021, Art. no. 116014.

[33] N. Diaz, H. R. Chacon, and H. A. Fuentes, "High-dynamic range compressive spectral imaging by grayscale coded aperture adaptive filtering," *Ingeniería e Investigación*, vol. 35, no. 3, pp. 53–60, 2015.

[34] N. Diaz, C. Hinojosa, and H. Arguello, "Adaptive grayscale compressive spectral imaging using optimal blue noise coding patterns," *Opt. Laser Technol.*, vol. 117, pp. 147–157, 2019.

[35] N. Diaz, H. Rueda, and H. Arguello, "Adaptive filter design via a gradient thresholding algorithm for compressive spectral imaging," *Appl. Opt.*, vol. 57, no. 17, pp. 4890–4900, Jun. 2018.

[36] G. deI. Computacional, "Hyper remote sensing scenes," [Online]. Available: http://www.ehu.eus/ccwintco/index.php/Hyperspectral_Remote_Sensing_Scenes#Pavia_Centre_and_University

[37] C. Hinojosa, J. M. Ramirez, and H. Arguello, "Spectral-spatial classification from multi-sensor compressive measurements using superpixels," in *Proc. IEEE Int. Conf. Image Process.*, 2019, pp. 3143–3147.

[38] D. Hong, N. Yokoya, J. Chanussot, and X. X. Zhu, "An augmented linear mixing model to address spectral variability for hyperspectral unmixing," *IEEE Trans. Image Process.*, vol. 28, no. 4, pp. 1923–1938, Apr. 2019.

Nelson Diaz (Member, IEEE) received the B.Sc. (Eng.) degree in computer science engineering, the M.Sc. degree in computer science, and the Ph.D. degree in engineering with emphasis in electronic from the Universidad Industrial de Santander, Bucaramanga, Colombia, in 2012, 2015, and 2020, respectively.

Currently, he holds a Postdoctoral position with the Pontificia Universidad Católica de Valparaíso (PUCV), Santiago, Chile, under the supervision of Prof. Esteban Vera. His research interests include high-dimensional signal processing, sparse image representation, adaptive sensing, compressive video, and spectral image classification.

Juan Ramirez (Member, IEEE) received the B.S. degree in electrical engineering, the M.S. degree in biomedical engineering, and the Ph.D. degree in applied sciences from the Universidad de Los Andes, Mérida, Venezuela, in 2002, 2007 and 2017, respectively.

He has been a Professor with the Electrical Engineering Department, Universidad de Los Andes, Venezuela, from 2004 to 2019. He was a postdoctoral fellow with the Department of Computer Science, Universidad Industrial de Santander, Colombia, from 2017 to 2019. He is currently a Got EnergyTalent GET-COFUND Marie Sklodowska-Curie Actions postdoctoral fellow at the Department of Computer Science at the Universidad Rey Juan Carlos, Spain. His research interest includes multi-sensor feature fusion, data fusion, and spectral image classification.

Esteban Vera (Member, IEEE) received the B.S. degree and Engineering Diploma in electronics engineering, and the M.S. and Ph.D. degrees in electrical engineering from the Universidad de Concepcion, Concepcion, Chile, in 1996, 1999, 2003, and 2010, respectively.

From 2001 to 2007, he worked as an Electronics Engineer for different large telescope projects, first with the Paranal Observatory, Cerro Paranal, Chile, and then with the Gemini Observatory, Vicuna, Chile. In 2010, he was a Postdoctoral Research Associate with the University of Arizona, Tucson, AZ, USA, and in 2013, he became a Research Scientist with Duke University, Durham, NC, USA. In 2016, he joined the School of Electrical Engineering, Pontificia Universidad Católica de Valparaíso, Valparaíso, Chile, where he is currently an Associate Professor. His research interests include computational imaging, compressed sensing, inverse problems, signal processing, machine learning, and the development of scientific and astronomical instrumentation.

Dr. Vera is a Member of the SPIE and a Senior Member of the OSA.

Henry Arguello (Senior Member, IEEE) received the B.Sc. Eng. degree in electrical engineering, the M.Sc. degree in electrical power from the Universidad Industrial de Santander, Bucaramanga, Colombia, in 2000 and 2003, respectively, and the Ph.D. degree in electrical engineering from the University of Delaware, Newark, DE, USA, in 2013.

He is currently an Associate Professor with the Department of Systems Engineering, Universidad Industrial de Santander. In first semester 2020, he was a Visiting Professor with Stanford University, Stanford, CA, USA, funded by Fulbright. His research interests include high-dimensional signal processing, optical imaging, compressed sensing, hyperspectral imaging, and CI.